

## DIFFUSE X-RAY EMISSION FROM THE SUPERBUBBLES N 70 AND N 185 IN THE LARGE MAGELLANIC CLOUD

REYES-ITURBIDE J.<sup>1</sup>, ROSADO, M.<sup>2</sup>, RODRÍGUEZ-GONZÁLEZ, A.<sup>1</sup>, VELÁZQUEZ P. F.<sup>1</sup>, SÁNCHEZ-CRUCES M.<sup>2</sup>, AND AMBROCIO-CRUZ, P.<sup>3</sup>.

*Draft version September 21, 2021*

### ABSTRACT

We present a study of the diffuse X-ray emission from superbubbles N 70 (DEM L301) and N 185 (DEM L25) located in the Large Magellanic Cloud, based on data from the XMM-Newton Satellite. We obtained spectra and images of these objects in the soft X-ray energy band. These X-ray spectra were fitted by a thermal plasma model, with temperatures of  $2.6 \times 10^6$  K and  $2.3 \times 10^6$  K, for N 70 and N 185, respectively. For N 70, images show that X-ray emission comes from the inner regions of the superbubble, when we compare the distribution of the X-ray and the optical emission; while for N 185, the X-ray emission is partially confined by the optical shell. We suggest that the observed X-ray emission is caused by shock-heated gas, inside of the optical shells. We also obtained X-ray luminosities which exceed the values predicted by the standard analytical model. This fact shows that, in addition to the winds of the interior stars, it is necessary to consider another ingredient in the description, such as a supernova explosion, as has been proposed in previous numerical models.

*Subject headings:* ISM: bubbles — ISM: H II regions — ISM: supernova remnants — stars: winds, outflows — galaxies: Magellanic Clouds — X-rays: ISM

### 1. INTRODUCTION

Massive stars transfer energy into the interstellar medium (ISM) in two ways during their lifetime: by radiative luminosity ( $L_*$ ) and by mechanical luminosity due to winds ( $L_w$ )— where  $L_w = \frac{1}{2} \dot{M}_w v_w^2$ ,  $\dot{M}_w$  is the mass loss rate and  $v_w$  is the wind terminal velocity—. In the “single scattering upper limit” approximation, which assumes that the momentum of the wind is equal that of the radiation, the mechanical luminosity of the stellar wind is less than one per cent of the stellar radiative luminosity,  $L_w/L_* = \frac{1}{2} v_w/c \lesssim 0.002$ , for a typical terminal velocity of winds from early-type stars (corresponding to  $v_w = 1000 \text{ km s}^{-1}$  and  $\dot{M}_w = 10^{-6} M_\odot \text{ yr}^{-1}$ ), and  $c$  is the speed of light. However, mechanical luminosity transfers energy to the interstellar medium (ISM) more efficiently. A classical example is found in OB associations (OBAs), which are composed of early-type massive stars that contain strong stellar winds, which in turn produce shock waves that sweep up the surrounding ISM, creating a superbubble (SB) around the OBA. The standard model (Weaver et al. 1977) describes these SBs as structures that consist of a shell of swept-up ISM, cool and bright in optical emission lines, that contains shock-heated gas emitting X-rays in its interior.

The standard model has been tested with observations of the kinematics and the X-ray emission of bubbles and superbubbles. Of particular relevance are the studies of SBs in the Large Magellanic Cloud (LMC) that have large-diameter shells, which in several cases are larger

than predicted by the standard model. Chu & Mac Low (1990) and Wang & Helfand (1991) found that most SBs had X-ray luminosities an order of magnitude higher than predicted by this model. Nevertheless, there are superbubbles with luminosities consistent with the predictions of the standard model. Oey (1996b) –based on observations by Rosado et al. (1981), Rosado et al. (1982) and Rosado (1986)– proposed two SB categories in terms of dynamical data: high-velocity and low-velocity superbubbles, latter type being more consistent with the standard model. Oey (1996b) concluded that X-ray emitting SBs with high expansion velocities and intermediate [S II]/[H  $\alpha$ ] line-ratios ( $\geq 0.5$ ) cannot be explained by the mechanical energy of stellar winds alone, and must be associated with supernova explosions that occurred in their interiors. The energy released by the supernova explosion would be an additional source of heating for the gas inside the superbubble, which would explain the observed X-ray excess. At the same time, the explosion would produce an acceleration of the shell that could explain the high expansion velocities observed. In a previous work (Rodríguez-González et al. 2011) it has been confirmed the high expansion velocities in the models in which a supernova event has taken place. For instance, the Gum Nebula is a case in which a supernova explosion can explain the X-ray emission (Leahy et al. 1992). However, as discussed in Rosado (1986) the detection of non-thermal radio emission is essential to have a definitive confirmation of the presence of a supernova remnant (SNR) in the SB.

In this work we study two SBs belonging to the high-velocity type: the N 70 and N 185 (both in the LMC). This characteristic makes these two superbubbles provide excellent laboratories in which to study the X-ray emission.

The superbubble N 70 (DEM L301) is an almost circular shell, about 100 pc in diameter. It contains the OBA LH 114 (Lucke & Hodge 1970), with more than 1000

<sup>1</sup> Instituto de Ciencias Nucleares, Universidad Nacional Autónoma de México, Apdo. Postal 70-543, D.F. México

<sup>2</sup> Instituto de Astronomía, Universidad Nacional Autónoma de México, Apdo. Postal 70-264, C.P. 04510, México, D.F., México

<sup>3</sup> Instituto de Ciencias Básicas e Ingeniería, Universidad Autónoma del Estado de Hidalgo, Ciudad Universitaria, Km 4.5 Carretera Pachuca-Tulancingo; Col. Carboneras, C.P. 42184, Mineral de la Reforma, Hgo., México.

stellar sources (The SIMBAD Astronomical Database); of these, seven are O-type stars (Oey 1996a). The mean age of this star association is about 5 Myr, a sufficient time for the first supernova explosion to occur. While radio observations are inconclusive about the non-thermal character of its radio continuum emission (Milne et al. 1980), a subsequent work by (Filipovic et al. 1998) reported a spectral index  $\alpha = -0.02$  which is larger than the typical  $\alpha = -0.43$  value for SNRs. Observations in the optical and X-ray bands have found evidence of a supernova explosion inside the superbubble (Rosado et al. 1981). Rosado et al. (1981) and Georgelin et al. (1983) obtained intermediate  $[S\ II]/[H\ \alpha]$  line-ratios in N 70, larger than those typical of photoionized HII regions, but lower than those typical of SNRs in the LMC. The range of values found in the outer filamentary shell is  $([0.8-2.0])$ , are close to the range of excitation in some of the supernova remnants observed in the LMC (Skelton et al. 1999). These line ratios can be explained by models with shock velocities of about  $40-70\text{ km s}^{-1}$ , in agreement with the measured expansion velocity of this superbubble. The high expansion velocity is in contradiction with the standard model (Oey et al. 1996b). Using archival data from the Einstein observatory, Chu & Mac Low (1990) reported an X-ray luminosity of N 70 an order of magnitude higher than predicted by the classical wind-blown bubbles model.

The superbubble N 185 (DEM L25) is very similar to N 70. N 185 has a spherical shape, with a diameter between 92 and 112 pc. Rosado et al. (1982) measured an expansion velocity of  $70\text{ km s}^{-1}$  for this superbubble. N 185 contains an OB association in its interior, consisting of more than 800 stellar sources (The SIMBAD Astronomical Database); where only one is an O-type star (Oey 1996a). The likelihood that it had some additional massive stars in the past, along the high expansion velocity, and the intermediate  $[S\ II]/[H\ \alpha]$  line-ratio (Rosado et al. 1982; Georgelin et al. 1983) suggest that this superbubble could have originated from a supernova explosion, or explosions. Radio observations have reported a spectral index  $\alpha = -0.67$ , which is typical of SNR candidates (Filipovic et al. 1998). N 185 was detected by ROSAT, with an X-ray luminosity of  $L_X \sim 1.8 \times 10^{35}\text{ erg s}^{-1}$  in Oey (1996a); this is higher than what is expected from standard model predictions.

To unravel the origin of these high-velocity superbubbles, we will focus our attention to their X-ray emission, now observed with more sensitive instruments such as XMM-Newton observatory. We selected these two SBs because of their high expansion velocities, their high  $[S\ II]/[H\ \alpha]$  line-ratios, and their X-ray excess. A detailed study of the X-ray emission could help us to determine if stellar winds alone are the origin of the large diameter shells, or if supernovae are required to produce the large shells. If supernova explosions have occurred in their interiors, then the X-ray emission might allow us to determine the relative contributions to the bubble expansion from the stellar winds and from the supernova explosions.

Our study of diffuse X-ray emission from SBs N 70 and N 185 is made with archival data from XMM-Newton observations. This paper is organized in the following way: In Section 2 we present a brief overview to the theory

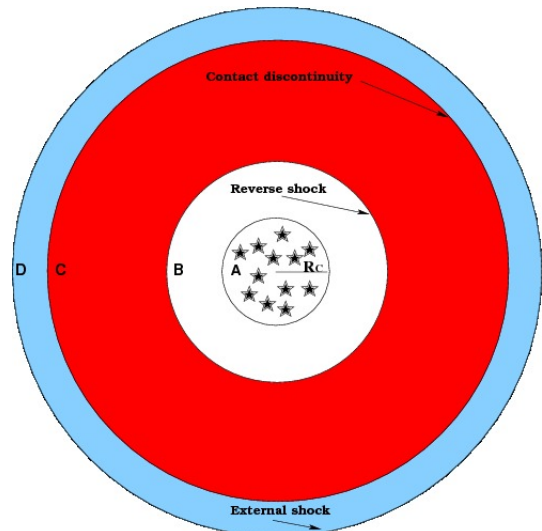


FIG. 1.— A generalization of the standard model (Weaver et al. 1977) conceived for a single star. Schematic structure of a superbubble produced by an OBA : (A) star cluster region, (B) free-wind region, (C) shocked-wind region, and (D) shocked-ISM region.

of superbubbles. Section 3 we present the data and describe its reduction. Sections 4 and 5 are dedicated to the observational results for the SBs N 70 and N 185, respectively. Finally, in Section 6 we give a discussion and our conclusions.

## 2. SUPERBUBBLE DYNAMICS AND SOFT X-RAY EMISSION

The standard model used to describe the structure of SBs is based on the original model of (Weaver et al. 1977), which describes the structure produced by the interaction of a wind of a single star with its environment, and it was later extended to include the winds of several stars in a OBA (Chu et al. 1995). The mechanical energy that the stars of the OBA deposit to the ISM in the form of stellar winds, is given by

$$L_w = \sum_{i=1}^N \frac{1}{2} \dot{M}_{w,i} v_{w,i}^2, \quad (1)$$

where  $\dot{M}_{w,i}$  and  $v_{w,i}$  are the mass-loss rate and the wind terminal velocity of the  $i$ th star, respectively, and  $N$  is the total number of stars. The interaction of this winds with ISM creates a superbubble structure with the following four regions (see Figure 1):

- (A) An inner zone where the stars are located and inject their winds. This region is delimited by the OBA radius  $R_C$ . Outside this region a common OBA wind is established.
- (B) A free-wind zone is the region between the OBA radius and the reverse shock. This region is filled by the unperturbed stellar OBA wind.
- (C) A shocked OBA wind zone located between a reverse shock (or inner shock) and the contact discontinuity.
- (D) An external zone, between the contact discontinuity and the external shock. This region contains

shocked ISM material that has been swept by the external shock.

In zone A, stellar winds of the massive stars collide with each other, thermalizing all the gas injected inside the cluster volume forming a common OBA wind –for this to be possible  $R_C \ll R$ , where  $R$  is the radius of superbubble–. The OBA wind expands freely inside zone B. Zone C is formed by gas of the stellar cluster wind that has been shocked by the inner or reverse shock. This outflow is thermalized and emits in soft X-ray energy range. Finally, zone D is formed by shocked-ISM gas emitting in optical; it is the densest zone according to the standard model. This description corresponds to the intermediate stage of evolution of the superbubble, there are important radiative losses in the region (D) but in region (C) there are small; and in the contact discontinuity that separates them thermal conduction transports heat due to the large temperature gradient between the regions (C) and (D) which have temperatures of  $10^6$  and  $10^4$ , respectively.

The equations that described the dynamics of the shell or region (D) according to the Weaver et al. (1977) model are:

$$R = (42 \text{ pc}) L_{w37}^{1/5} n_0^{-1/5} t_6^{3/5}, \quad (2)$$

$$V = \frac{dR}{dt} = (0.59 \text{ km s}^{-1}) R_{\text{pc}} / t_6. \quad (3)$$

$R$  and  $V$  are the radius and expansion velocity of the SB; where  $R_{\text{pc}}$  is the radius in units of pc,  $L_{w37}$  is the mechanical luminosity of the OBA in units of  $10^{37}$  erg  $\text{s}^{-1}$ ,  $n_0$  and  $t_6$  are the number density of the ambient medium in units of  $\text{cm}^{-3}$  and the age of the bubble in  $10^6$  years, respectively.

The X-ray luminosity of a spherically symmetric gas distribution is given by the integral X-ray emissivity in the layer of shocked stellar wind –region (C)–:

$$L_X = \int n^2(R) \Lambda_X(Z, T) d^3R, \quad (4)$$

where  $R$  is the radial coordinate,  $n(R)$  is the numerical density, and  $\Lambda_X(Z, T)$  is the X-ray emissivity as a function of its temperature and metallicity. The X-ray luminosity that arises from the shocked gas (zone C) in the superbubble evolving inside a homogeneous ISM can be estimated by integrating Eq (4) from center to radius  $R_{\text{max}}$  where the temperature drops to the minimum (i.e.,  $T(R_{\text{max}}) = T_{\text{min}}$ ). As presented by Weaver et al. (1977) and Chu et al. (1995), the integral can be written as:

$$L_X = 1.1 \times 10^{35} I(\tau) \xi L_{w37}^{33/35} n_0^{17/35} t_6^{19/35} (\text{erg s}^{-1}), \quad (5)$$

where  $\xi$  is the gas metallicity, and

$$I(\tau) = \frac{125}{33} - 5\tau^{1/2} + \frac{5}{3}\tau^3 - \frac{5}{11}\tau^{11/3}, \quad (6)$$

with

$$\tau = 0.16 L_{w37}^{-8/35} n_0^{-2/35} t_6^{6/35}. \quad (7)$$

The expression for the X-ray luminosity –Equation(5)– is practical because  $L_x$  can be derived from physical parameters obtained from observations such as ISM density,

expansion velocity and the size of the SB, and the mechanical energy of the OBA wind.

### 3. XMM-NEWTON DATA AND DATA REDUCTION

Superbubbles N 70 and N 185 were observed with The European Photon Imaging Camera (EPIC), on board of the XMM-Newton observatory. EPIC consists of two Metal Oxide Semi-conductor (MOS) CCD arrays (MOS1 & MOS2, Turner et al. 2001) and a pn-CCD (Strüder et al. 2001). A summary of the observations is given in Table 1. The EPIC MOS cameras were operated in the Prime Full-Window Mode and the EPIC pn camera was operated in the Extended Prime Full-Window Mode. Two of the cameras contain seven MOS CCDs, while the third uses twelve PN CCDs, defining a circular field of vision (FOV) of  $\sim 30'$  in diameter, allowing the inclusion of the entire superbubbles (sizes between  $6' - 10'$ ) in one pointing. In both observations, a medium filter was used to block ultraviolet photons (Villa et al. (1998) and Stephan et al. (1996)). The XMM-Newton pipeline products were processed using the XMM-Newton Science Analysis Software (SAS version 11.0.0).

Since the emission from these superbubbles is extended, the data were processed with the XMM-Newton Extended Source Analysis software package (XMM-ESAS) (Snowden et al. 2008) for the analysis of EPIC MOS and pn observations. XMM-ESAS documentation can be found at the SAS Package documentation web pages: <http://xmm.esac.esa.int/sas/current/howtouseesas.shtml>. This package automatically filters times of high background contamination. The resulting effective exposure times are given in Table 1.

After filtering the event files, we created mosaic images of the EPIC cameras. We used the “cheese” task to identify point sources and remove them. The package includes tasks to create and model the non-cosmic background, correct the exposures and subtract the backgrounds. We generate combined images (with a pixel size of  $2.5''$ ) of the EPIC cameras in the ( $[0.4 - 1.5]$ ) keV bands; there is no significant emission of the diffuse X-ray emission above 2.0 keV for both superbubbles. Finally, they were smoothed as described in Section 4.1 and 5.1.

A good background knowledge is crucial for the spectral analysis. For a point source, a local background extracted from a neighboring region can be used. In the case of a diffuse source, as in the case of SBs N 70 and N 185 corresponding to an area of diffuse X-ray emission that covers one third of the XMM-Newton FOV –filling entirely CCD#1 or the central CCD of EPIC MOS–, it is inappropriate to estimate the local background from the same data; many effects can be produced due to differences in chip position. The high-energy particles that interact with material surrounding the detector produce fluorescence, which varies with position on the detector, especially for the PN detector. In addition, the spectral response depends on the position on the detector. To estimate the background of diffuse sources, the XMM-Newton EPIC Background working group has created the so called blank sky data for each EPIC (Carter & Read 2007). The blank sky data have been merged with data from different pointings after the point sources were eliminated. This data set consists in the detector background and an average cosmic X-ray background. In this paper we used the blank sky data obtained by XMM-

Newton EPIC Background Working Group (Request id: 0573-0575) in the direction of the SBs N70 and N185.

Before extracting the spectra, we have first corrected both the observed data and the blank sky data for vignetting using the XMMSAS command `evigweight`. The spectra of the diffuse X-ray emission from N70 and N185 were extracted from the event files of the EPIC cameras. These spectra were extracted from a circular region encompassing the entire superbubble, while the background spectrum is extracted from the blank sky data at the same location on the detector as the source spectrum. For this we use the script `skycast`, which converts the detector coordinates of the XMM EPIC background into sky coordinates, using the pointing direction of the observation. Finally, the spectra are grouped with a minimum of 25 counts/bin.

#### 4. RESULTS FOR N70

##### 4.1. Images: X-ray brightness distribution

Figure 2 shows a mosaic of images in the  $([0.4 - 1.5])$  keV energy band in the direction of SB N70. The top-left panel displays a combined EPIC MOS1/2 and pn FOV image, which have been obtained by using the task `comb`. The top-right panel shows the combined EPIC smoothed (with a kernel of 80 counts) image, with a size of  $15' \times 15'$ , where the non-cosmic background was subtracted and the exposure has been corrected. Besides, several point sources have been identified and removed from this observation, which are indicated by small circular voids in this image. A  $15'$  square smoothed image is displayed in the bottom-left panel of Fig. 2, which is overlaid by the X-ray contours at  $3\sigma$ ,  $4\sigma$  and  $5\sigma$  above the cosmic background level. In order to analyze the spatial distribution of the soft X-ray emission, in the bottom-right panel we show a comparison between the  $H\alpha$  emission of N70, which was taken from the Magellanic Cloud Emission Line Survey (MCELS; Smith et al. 1998), and the X-ray emission (in black contours). We note that the soft X-ray emission is well-confined within the  $H\alpha$  shell. This spatial distribution suggests that the X-ray emission is produced by hot gas inside the optical superbubble. This distribution is recreated with an RGB image-panel (Figure 3) where the  $H\alpha$  emission is displayed in red and the diffuse soft X-ray is shown in green. Note the emission to the East, external to the optical superbubble, it is related to some sources found in the field of vision.

##### 4.2. Spectra and X-ray luminosity from diffuse emission

For spectral analysis of the EPIC MOS data, we used XSPEC version 12.5.0 (distributed with the HEASOFT 6.6.1 software). The spectra of the EPIC MOS1/2 and EPIC pn were extracted from a circular region encompassing entirely the N70 superbubble. The point sources inside this region were excluded. The background contribution was estimated from blank sky data for each EPIC-MOS1/2 and EPIC-PN; these contain both contributions (i.e., instrumental and cosmic). The background subtracted source spectra are shown in Figure 4. We present the EPIC MOS1/2 and pn spectra in the interval of energy  $([0.2 - 1.1])$  keV and  $([0.4 - 1.1])$ , respectively.

In order to obtain the physical conditions of the X-ray-emitting gas, the EPIC spectra were fitted simultaneously with a thermal model (APEC) (Smith et al.

2001) convolved with the interstellar absorption. The best fit gives a reduced  $\chi^2 = 1.3$  ( $\chi^2/d.o.f = 320.6/242$ ). We used a single absorbing column density via the photoelectric absorption model (PHABS Balucinska-Church & McCammon 1992), using reasonable values for the absorption column density,  $N_H = 5.0 \times 10^{20} \text{ cm}^{-2}$ , which is in agreement with the measures of column densities in the LMC direction, average  $N_H = 6.4 \times 10^{20} \text{ cm}^{-2}$  (Dickey & Lockman 1990). The chemical abundance was set to 0.3 times the solar abundance, i.e., the average value of the ISM in the LMC (Russell & Dopita 1992; Hughes et al. 1998). This best-fit has plasma temperatures of  $kT = 0.22$  keV. The observed total flux of the diffuse X-ray emission, corrected for absorption, is  $(0.7 \pm 0.1) \times 10^{-12} \text{ erg cm}^{-2} \text{ s}^{-1}$  in the  $[0.2 - 1.1]$  keV range, which corresponds to X-ray luminosity (at the LMC distance of 54 kpc, Feast (1999)) of  $2.4 \pm 0.4 \times 10^{35} \text{ erg s}^{-1}$ . The best-fit model is overplotted on the EPIC spectra with a solid curves in Figure 4, and the best-fit parameters are listed in Table 2.

#### 5. RESULTS FOR N185

##### 5.1. X-ray brightness distribution

Figure 5 shows an image mosaic of N185, in the  $([0.4 - 1.5])$  keV energy band, which is similar to that shown in Figure 2 for the case of N70. The combined EPIC MOS1/2 and pn FOV image is displayed in the top-left panel while in the top-right panel is shown the combined EPIC smoothed image (in this case with a kernel of 50 counts). The bottom-left panel show the smoothed X-ray image, which is overlaid by X-ray contours at  $5\sigma$ ,  $6\sigma$  and  $9\sigma$  above the cosmic background level. Finally, the comparison between  $H\alpha$  (color-scale) and X-ray (black contours) emission is shown in the bottom-right panel. As in Figure 2, the  $H\alpha$  emission was taken from the Magellanic Cloud Emission Line Survey (MCELS; Smith et al. 1998).

We note that, in the case of N185, the soft X-ray emission is only partially confined by the  $H\alpha$  shell, X-ray emission extends well beyond the optical shell to the southeast direction, where the optical shell appears bright and well defined, so it is probable that the gas is escaping towards the back of the SB.

This comparison is recreated with an RGB image (Figure 6) where  $H\alpha$  and soft X-ray emission are displayed in red and green, respectively.

##### 5.2. X-ray spectra and luminosity from diffuse emission

The same method was employed to extract the spectra of the diffuse emission and make the analysis of the superbubble N185. The spectra of the EPIC MOS1/2 and EPIC PN were extracted from a circular region encompassing the entirety of N185 superbubble. The point sources in this region were excluded from the analysis. The background contribution was estimated from blank sky data for each EPIC-MOS1/2 and EPIC-PN data. The background subtracted source spectra are shown in Figure 7. We present the EPIC MOS1 and pn spectra in the interval of energy  $([0.2 - 1.1])$  keV and  $([0.4 - 1.1])$ , respectively. Absorbed APEC model was used to fit this spectrum. Figure 7 displays both the observed spectra and the best-fit model spectrum. To obtain this best-fit model, with a reduced  $\chi^2 = 1.6$ ,

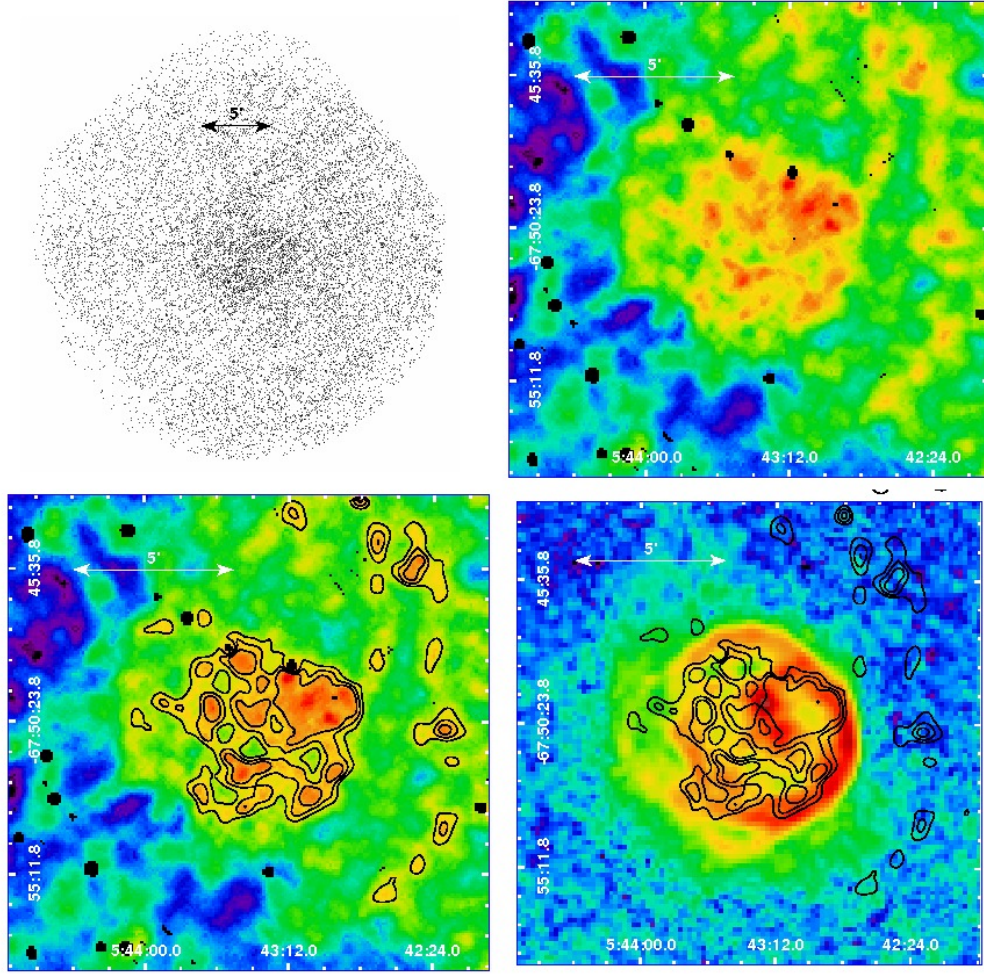


FIG. 2.— The mosaic EPIC images of N 70, in the  $([0.4 - 1.5])$  keV energy band. Top row: left, the raw data, combined EPIC MOS1/2 and pn image; right, the combined EPIC smoothed image. Bottom row: left, X-ray contours at  $3\sigma$ ,  $4\sigma$  and  $5\sigma$  above the cosmic background level are superposed onto the smoothed image; right, a comparison between the  $H\alpha$  emission of N 70, which was taken from the Magellanic Cloud Emission Line Survey (MCELS; Smith et al. 1998), and the X-ray emission (in black contours). Note the X-ray emission observed to the West, it is external to the optical superbubble, which is related to some field sources detected in this observation.

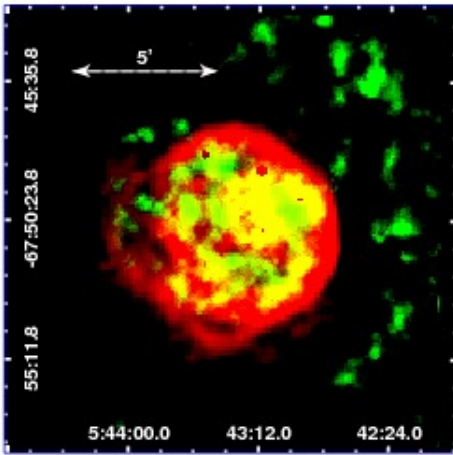


FIG. 3.— RGB image of N 70. MCELS image of  $H\alpha$  emission is shown in red, while the diffuse soft X-ray emission is displayed in green.

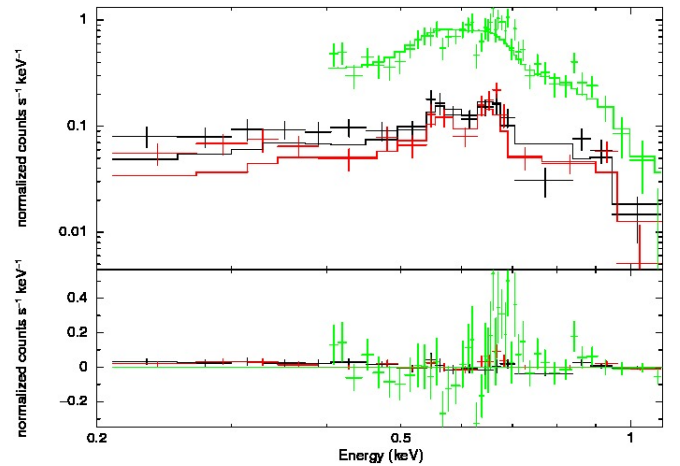


FIG. 4.— XMM-EPICs background subtracted source spectra of the diffuse X-ray emission from N70. The solid lines show the best-fit model. In black, red and green EPIC MOS1, MOS2 and PN, respectively.

we have set the chemical abundance at the LMC average values (i.e., 0.3 times solar abundance (Russell &

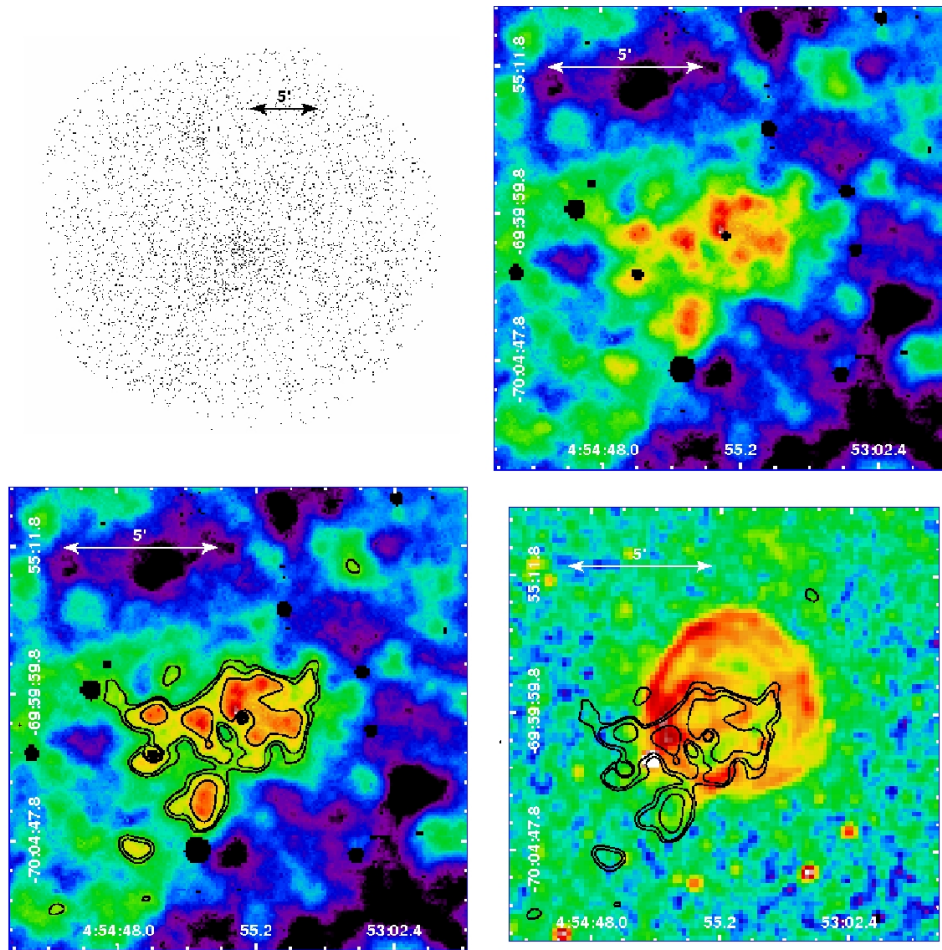


FIG. 5.— The mosaic EPIC images from N 185, in the  $([0.4 - 1.5])$  keV energy band. Top row: left, the raw data, combined EPIC MOS1/2 and pn image; right, the combined EPIC smoothed image. Bottom row: left, X-ray contours at  $5\sigma$ ,  $6\sigma$  and  $9\sigma$  above the cosmic background level are superposed onto smoothed image; a comparison between the  $H\alpha$  emission of N 185, which was taken from the MCELS (Smith et al. 1998), and the X-ray emission (in black contours).

Dopita 1992; Hughes et al. 1998)), and we used a column density value  $N_H = 5.0 \times 10^{20} \text{ cm}^{-2}$  in agreement with previous measurements of column densities in the LMC direction (Dickey & Lockman 1990). Plasma temperatures of  $kT = 0.20$  keV, the observed total flux of the diffuse X-ray emission, corrected for absorption, is  $(0.6 \pm 0.1) \times 10^{-12} \text{ erg cm}^{-2} \text{ s}^{-1}$  in the  $[0.2 - 1.1]$  keV range (see Table 3), which corresponds to X-ray luminosity (at the LMC distance of 54 kpc, Feast (1999)) of  $2.1 \pm 0.7 \times 10^{35} \text{ erg s}^{-1}$ .

## 6. DISCUSSION AND CONCLUSIONS

We conducted a detailed study based on XMM-Newton data of the SBs N 70 and N 185, in the LMC. We have generated both X-ray images and spectra of these objects. In both SBs, we find soft diffuse X-ray emission. Soft X-ray emission comes from the inner region of the SBs (i.e., interior to the optical shells). Our results show thermal spectra from SBs which are associated with the soft X-ray emission.

As discussed in Section 2, there is an analytical model that aims to explain the soft X-ray emission from bubbles and superbubbles (Weaver et al. 1977), and has become the standard model for SBs. According to this model,

the supersonic winds from massive (OB stars) interact with the interstellar medium forming an expanding cold shell ( $\sim 10^4$  K) with a hot interior ( $\sim 10^6$  K) of shocked wind. We have calculated the X-ray luminosity from superbubbles N 70 and N 185, using the Eq. (5). In this calculation we only take into account the stars that dominate the mechanical luminosity of the stellar cluster associated with these superbubbles (see Rosado et al. 1981, 1982; Oey 1996a). Using the high terminal velocities and mass loss rates of stars with similar spectral types and luminosities, and considering the average observational parameters for both superbubbles: an expansion velocity of  $70 \text{ km s}^{-1}$ , SB radius of 50 pc, and ambient density of  $0.1 \text{ cm}^{-3}$  (from Eq. 5), the soft X-ray luminosity is  $6 \times 10^{34} \text{ erg s}^{-1}$  for N 70 and  $5 \times 10^{33} \text{ erg s}^{-1}$  for N 185. From our observations we obtain an X-ray luminosity of  $2.4 \times 10^{35} \text{ erg s}^{-1}$  for N 70, and of  $2.1 \times 10^{35} \text{ erg s}^{-1}$  for N 185 (see Table 4). Therefore, the X-ray luminosity predicted by the standard model is four times lower than the observed values for N 70, and 40 times lower than observed for N 185. In this cases the standard model of wind-blown bubbles cannot explain the observed soft X-ray emission of these SBs.

In a previous work, Rodríguez-González et al. (2011)

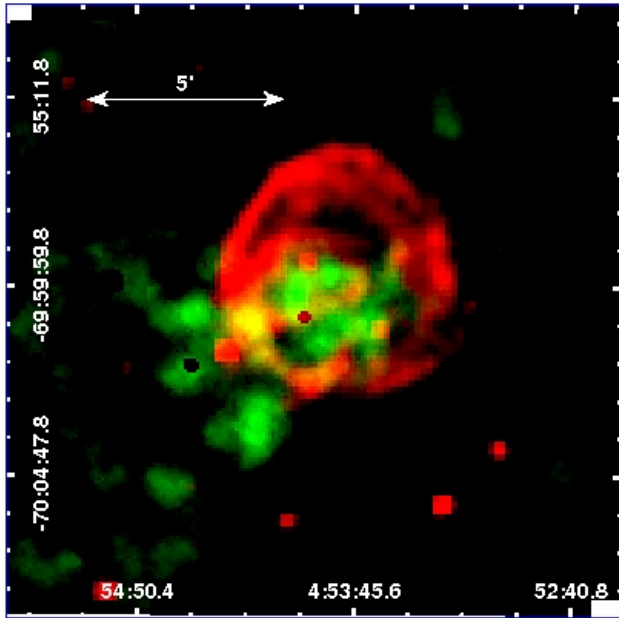


FIG. 6.— RGB image of N 185. As in Figure 5 the MCELS  $H\alpha$  and the diffuse soft X-ray emissions are displayed in red and green, respectively.

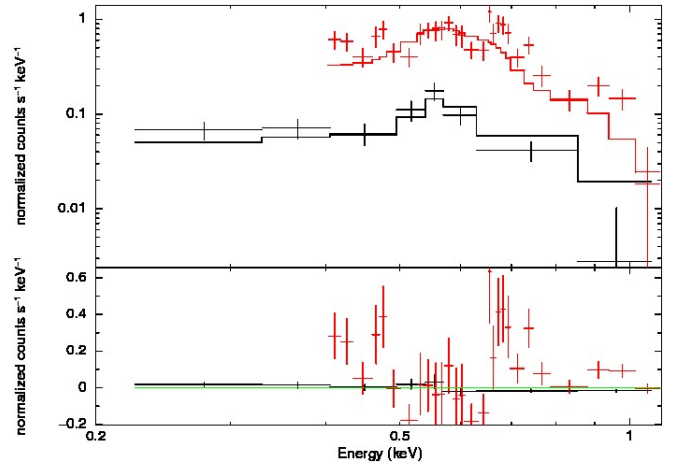


FIG. 7.— XMM-EPICs background subtracted source spectra of the diffuse X-ray emission from N 185. The solid lines show the best-fit model. In black EPIC MOS1 and PN in green.

carried out numerical models of the SB evolution applied to N 70. As does the standard model, their models predict that the primary X-ray emission will be in the soft X-ray band and that it has a thermal origin ( $\sim 10^6$  K). In that work several models were performed in order to reproduce the soft X-ray luminosity, the high expansion velocity and the large radius of this superbubble. The model including both a supernova explosion (absent in the standard model of Weaver et al. 1977) and the stellar winds fits quite well with the kinematics of the optical shell, and the excess of thermal X-ray emission of N 70. An X-ray luminosity of  $2 \times 10^{35}$  erg  $s^{-1}$  was obtained for this model, a value that agrees with the observed X-ray luminosity obtained for N 70 in this paper (see Table 4).

For N 185, the same arguments can be employed to justify the inclusion of a supernova, and indeed, non-thermal radio emission has been detected as mentioned in the Introduction. A supernova explosion is also consistent with the stellar population models for N 70 and N 185 presented by Oey (1996b), in which 13 and 15 massive stars, respectively, are found between 12 and  $40 M_{\odot}$ . A  $60 M_{\odot}$  star could be expected using a standard initial mass function for both superbubbles and, if formed with the rest of the cluster, it would already have exploded as an SN. Thus, the kinematics, the size and the excess soft X-ray emission of these SBs can be explained by a SN exploding in a wind-blown SB.

We thank F. De Colle for insightful discussions and acknowledge financial support from the PAPIIT-UNAM (IA101413-2). PFV and ARG acknowledge financial support by CONACyT grants 167611 and 167625, and DGAPA-PAPIIT grant IG100214.

#### REFERENCES

- Balucinska-Church, M., & McCammon, D. 1992, *ApJ*, 400, 699  
 Bamba, A., Ueno, M., Nakajima, H., & Koyama, K. 2004, *ApJ*, 602, 257  
 Carrera, F. J., Ebrero, J., Mateos, S., et al. 2007, *A&A*, 469, 27  
 Carter, J. A., & Read, A. M. 2007, *A&A*, 464, 1155  
 Chu, Y.-H., Chang, H.-W., Su, Y.-L., & Mac Low, M.-M. 1995, *ApJ*, 450, 157  
 Chu, Y.-H., & Mac Low, M.-M. 1990, *ApJ*, 365, 510  
 Cooper, R. L., Guerrero, M. A., Chu, Y.-H., Chen, C.-H. R., & Dunne, B. C. 2004, *ApJ*, 605, 751  
 Dennerl, K., Haberl, F., Aschenbach, B., et al. 2001, *A&A*, 365, L202  
 Dickey, J. M., & Lockman, F. J. 1990, *ARA&A*, 28, 215  
 Feast, M. 1999, *PASP*, 111, 775  
 Filipovic, M. D., Haynes, R. F., White, G. L., & Jones, P. A. 1998, *A&AS*, 130, 421

- Georgelin, Y. M., Georgelin, Y. P., Laval, A., Monnet, G., & Rosado, M. 1983, *A&AS*, 54, 459
- Hughes, J. P., Hayashi, I., & Koyama, K. 1998, *ApJ*, 505, 732
- Kaastra, J.S., & Mewe, R. 1993, *Legacy*, 3, 16
- Leahy, D. A., Nousek, J., & Garmire, G. 1992, *ApJ*, 385, 561
- Liedahl, D. A., Osterheld, A. L., & Goldstein, W. H. 1995, *ApJ*, 438, L115
- Lucke, P. B., & Hodge, P. W. 1970, *AJ*, 75, 171
- Maddox, L. A., Williams, R. M., Dunne, B. C., & Chu, Y.-H. 2009, *ApJ*, 699, 911
- Mateos, S., Saxton, R. D., Read, A. M., & Sembay, S. 2009, *A&A*, 496, 879
- Milne, D. L., & Haynes, R. F. 1980, *MNRAS*, 191, 469
- Morrison, R., & McCammon, D. 1983, *ApJ*, 270, 119
- Oey, M. S. 1996a, *ApJ*, 467, 666
- Oey, M. S. 1996b, *ApJ*, 465, 231
- Reynolds, S. P. 1998, *ApJ*, 493, 375
- Reynolds, S. P., & Keohane, J. W. 1999, *ApJ*, 525, 368
- Rodríguez-González, A., Velázquez, P. F., Rosado, M., et al. 2011, *ApJ*, 733, 34
- Rosado, M., Georgelin, Y. P., Georgelin, Y. M., Laval, A., & Monnet, G. 1981, *A&A*, 97, 342
- Rosado, M., Georgelin, Y. M., Georgelin, Y. P., Laval, A., & Monnet, G. 1982, *A&A*, 115, 61
- Rosado, M. 1986, *A&A*, 160, 211
- Russell, S. C., & Dopita, M. A. 1992, *ApJ*, 384, 508
- Skelton, B. P., Waller, W. H., Gelderman, R. F., et al. 1999, *PASP*, 111, 465
- Snowden, S. L., Mushotzky, R. F., Kuntz, K. D., & Davis, D. S. 2008, *A&A*, 478, 615
- Smith, R. C., et al. 1998, *Publ. Astron. Soc. Aust.*, 15, 163
- Smith, R. K., Brickhouse, N. S., Liedahl, D. A., & Raymond, J. C. 2001, *ApJ*, 556, L91
- Stephan, K.-H., Reppin, C., Hirschinger, M., Maier, H. J., Frischke, D., Fuchs, D., Mueller, P., & Guertler, P. 1996, *Proc. SPIE*, 2808, 421
- Strüder, L., et al. 2001, *A&A*, 365, L18
- Turner, M. J. L., et al. 2001, *A&A*, 365, L27
- Villa, G. E., et al. 1998, *IEEE Transactions on Nuclear Science*, 45, 921
- Wang, Q., & Helfand, D. J. 1991, *ApJ*, 373, 497
- Watson, M. G., Schröder, A. C., Fyfe, D., et al. 2009, *A&A*, 493, 339
- Weaver, R., McCray, R., Castor, J., Shapiro, P., & Moore, R. 1977, *ApJ*, 218, 377
- Yamaguchi, H., Sawada, M., & Bamba, A. 2010, *ApJ*, 715, 412

TABLE 1  
LOG OF OBSERVATIONS IN THIS PAPER.

Target name	Obs ID	Position (J2000) (RA, DEC)	Date (yyyy/mm/dd)	Time Exposure (ks)	Effective Exposure (ks)
N 70	0503680201	(05 <sup>h</sup> 43 <sup>m</sup> 25 <sup>s</sup> .0, -67 <sup>d</sup> 51 <sup>m</sup> 12 <sup>s</sup> .0)	2008/01/26	38.3	21.0(MOS)/12.5 (pn)
N 185	0503680101	(04 <sup>h</sup> 53 <sup>m</sup> 47 <sup>s</sup> .40, -69 <sup>d</sup> 59 <sup>m</sup> 15 <sup>s</sup> .0)	2008/03/10	20.5	8.3 (MOS)/5.5 (pn)

TABLE 2  
X-RAY FROM N 70: BEST-FIT PARAMETERS OF THE SPECTRAL MODEL

Model	$N_H$ $\times 10^{20} \text{ cm}^{-2}$	$kT$ keV	$n_e n_p V$ $\times 10^{58} \text{ cm}^{-3}$
Absorption	5.0	-	
Apec		0.22(0.21-0.23)	3.4 $\pm$ 0.1
Flux=(0.7 $\pm$ 0.1) $\times 10^{-12} \text{ erg cm}^{-2} \text{ s}^{-1}$			
$\chi^2/d.o.f = 320.57/242$			

TABLE 3  
X-RAY FROM N 185: BEST-FIT PARAMETERS OF THE SPECTRAL MODEL

Model	$N_H$ $\times 10^{20} \text{ cm}^{-2}$	$kT$ keV	$n_e n_p V$ $\times 10^{58} \text{ cm}^{-3}$
Absorption	5.0	-	
Apec		0.20(0.19-0.21)	3.2 $\pm$ 0.4
Flux=(0.6 $\pm$ 0.2) $\times 10^{-12} \text{ erg cm}^{-2} \text{ s}^{-1}$			
$\chi^2/d.o.f = 151.02/94$			

TABLE 4  
SOFT X-RAY LUMINOSITIES, COMPARISON BETWEEN OBSERVED AND PREDICTED OF THE SBs

	XMM-Newton observation $L_X$ ( $10^{35} \text{ erg s}^{-1}$ )	Predicted (Weaver et al.) $L_X$ ( $10^{35} \text{ erg s}^{-1}$ )	Numerical model* $L_X$ ( $10^{35} \text{ erg s}^{-1}$ )
N 70	2.4 $\pm$ 0.4	0.6	2.0
N 185	2.1 $\pm$ 0.7	0.05	